



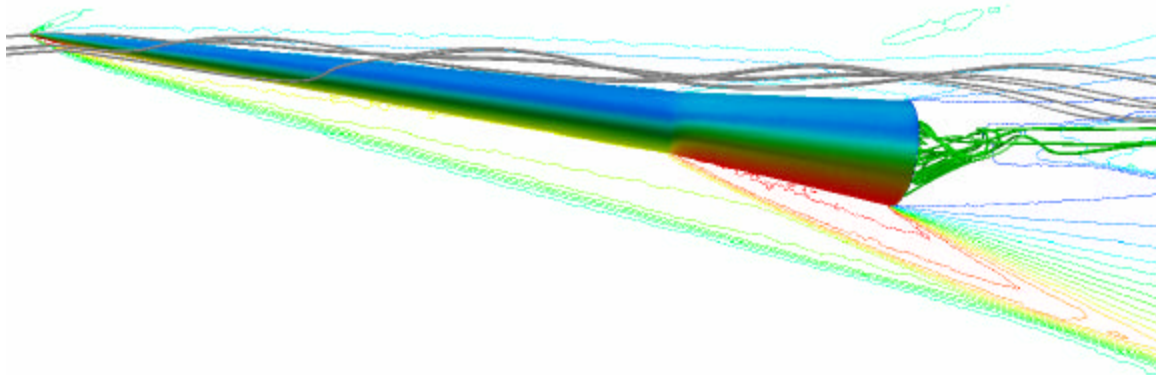
AIAA 2001-4430

## Comparison of Numerical Methods for an Elliptic Section Projectile

James R. Forsythe  
United States Air Force Academy  
U.S. Air Force Academy, CO 80840

John A. Edwards  
Dstl Fort Halstead  
Sevenoaks Kent TN14 7BP

Jubaraj Sahu  
U.S. Army Research Laboratory  
Aberdeen Proving Ground, MD 21005



**AIAA Atmospheric Flight Mechanics  
Conference & Exhibit  
August 6-9, 2001/Montréal, Canada**



# Comparison of Numerical Methods for an Elliptic Section Projectile

James R. Forsythe\*

U.S. Air Force Academy  
USAF Academy, CO 80840

John A. Edwards†

Dstl Fort Halstead  
Sevenoaks Kent TN14 7BP

Jubaraj Sahu‡

U.S. Army Research Laboratory  
Aberdeen Proving Ground, MD 21005

## Abstract

This paper presents a comparison of several computational fluid dynamics codes applied to a power-law elliptic cross-section projectile at Mach 4.0. Experimental data is used primarily as a basis of comparison, supplemented by limited free flight results. Four codes were used – CHASM, CFD++, Cobalt<sub>60</sub>, and ZNSFLOW. The methods used included the solution of the parabolized and full Navier Stokes equations on structured and unstructured grids using several different turbulence models. All codes were seen to predict normal forces and moments to within a few percent. Discrepancies were noticed in the center of pressure predictions for one code. Only the full Navier Stokes codes could solve for free flight axial force because of the need to solve for base drag. The predictions of axial force compared to the wind tunnel were within about 10%. Larger differences were seen at free flight conditions. Computation times were discussed with the parabolized Navier Stokes having a clear advantage.

## List of Symbols

$A$	=	cross section area of the model and reference area ( $A = p * d_{maj} * d_{min}$ )
$cg$	=	center of gravity
$C_m$	=	pitch moment coefficient ( $C_m \equiv \frac{m}{\bar{q} A d_{ref}}$ )
$C_n$	=	yaw moment coefficient ( $C_n \equiv \frac{n}{\bar{q} A d_{ref}}$ )
$C_x$	=	axial force coefficient ( $C_x \equiv \frac{X}{\bar{q} A}$ )
$C_{x_0}$	=	zero yaw axial force coefficient

$C_Y$	=	yaw force coefficient ( $C_Y \equiv \frac{Y}{\bar{q} A}$ )
$C_Z$	=	normal force coefficient ( $C_Z \equiv \frac{Z}{\bar{q} A}$ )
$d_{maj}$	=	major diameter of the model
$d_{min}$	=	minor diameter of the model
$d_{ref}$	=	reference diameter of the model
$e$	=	elliptic cross-section eccentricity
$k$	=	model surface constant
$l$	=	model length
$l, m, n$	=	roll, pitch, and yaw moment about projectile cg
$\bar{q}$	=	dynamic pressure
$r$	=	radius of model surface
$x_{c.p.}$	=	location of center of pressure measured from nose
$X, Y, Z$	=	axial, yaw, and normal body forces
$z$	=	vertical position coordinate
$\alpha$	=	pitch angle
$\beta$	=	yaw angle
$\varphi$	=	angular coordinate of model surface

## Introduction

### Background

The use of highly maneuvering projectiles for increased lethality is being explored for future weapon systems in various scenarios (e.g., air-to-air, air-to-ground, etc.).<sup>1</sup> Additionally, non-axisymmetric projectiles have been shown to generate large amounts of lift than conventional circular projectiles.<sup>2</sup> However, high speed (Mach > 3.0) maneuvering projectiles have been extremely difficult to attain. Aside from the control system responsible for maneuvering the projectile, the aerodynamics of such configurations at high speeds are still complex due to strong cross-flow influences and flow separation.<sup>3,4,5</sup>

The work documented herein is part of an international collaborative effort specifically dealing with high-speed weapon integration. Under this collaboration, complementary technical tasks are performed to provide a greater overall understanding

\* Assistant Professor, Member AIAA

† Senior Principal Consultant, Associate Fellow AIAA

‡ Aerospace Engineer, Associate Fellow AIAA

of the technology. Comparisons between predictive and experimental data will highlight deficiencies and provide confidence in future system design studies.

### Objectives

The overall objectives of the collaborative research effort are:

- To assess the application and relevance of high-speed maneuvering projectiles
- To develop and validate predictive methodologies for these configurations

This paper will present only the aerodynamic results obtained from several numerical simulations, using experimental data and free flight tests as a basis for comparison. The sole configuration studied in this paper is a 0.75 power-law elliptic cross-section projectile.

### Approach

A suitable configuration was selected to perform the aerodynamic analysis. The UK H3P78 was chosen as a final design of the collaborative effort. Wind tunnel testing was provided by Fournier et al<sup>6</sup>. Limited flight test data was provided by Dupuis<sup>7</sup>. Four codes were used – CHASM, CFD++, Cobalt<sub>60</sub>, and ZNSFLOW. The methods used included the solution of the parabolized and full Navier Stokes equations on structured and unstructured grids using several different turbulence models. The codes were applied in a “blind” fashion to test their reliability in a predictive mode – i.e. the users of the codes had no knowledge of the wind tunnel or flight test results. The result of this study builds confidence in applying the CFD techniques to predict the performance of slender projectiles.

### Model Geometry

The configuration studied in this effort is designated as the “H3P78” and is depicted in Figure 1. The H3P78 is a three-quarters power-law projectile with a 0.6 aspect elliptic cross-section. The cross-sectional variation of the body that is given by the power law is

$$r = kx^{0.75} \quad (1)$$

where  $k$  is a constant for constant  $q$  and the  $x$ -axis origin is at the nose of the projectile. The H3P78 length is given as 405 mm and the major base diameter is 83 mm<sup>2</sup>. The projectile has a 6° flare of length 105mm, as shown in Figure 1 Note that the length, major base diameter, flare angle and length,

and ellipticity (given as 0.6) are all that is required to define this shape.

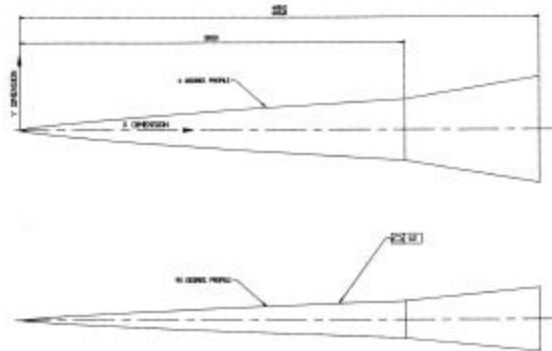


Figure 1. H3P78 model geometry

### Numerical Analysis

#### CHASM

The solver employed in this study – CHASM (coning, helical and spinning motion), developed by Dstl and Cranfield University<sup>8,9,10,11,12</sup>, solves the Parabolized Navier-Stokes (PNS) equations in either inertial or non-inertial reference frames using an iterative finite volume approach within a structured meshed domain. The perfect gas law is assumed together with Sutherland’s model for molecular viscosity.

The solver has been validated for supersonic projectile configurations<sup>11,12</sup> at incidence and developments of this approach have recently been successfully applied to external and internal hypersonic aerodynamic problems<sup>13,14</sup>.

The numerical integration procedure yields cell average flow properties, assigned to the cell centres of each hexahedral cell. The flux vectors are evaluated at the cell interfaces as viscous and inviscid contributions. In the crossflow plane the inviscid fluxes are calculated using Osher’s approximate Riemann solver<sup>15</sup>. The viscous and heat fluxes are evaluated using central differences.

The calculation involves the solution on successive crossflow planes from the inflow plane to the downstream boundary. Second order accuracy, outside the boundary layer, in the streamwise marching direction is achieved using a non-monotone, primitive variable extrapolation scheme.

Third order spatial accuracy in the crossflow plane is attained using the MUSCL variable extrapolation procedure and a suitable slope limiter. The solution on each streamwise plane is initialized using the solution directly upstream and the equations are solved using a pseudo time marching scheme based on Approximate Factorization (AF). The parabolizing approximation of Vigneron et al<sup>16</sup> was

employed, whereby a component of the streamwise gradient is neglected. Turbulent viscosity is modeled using the algebraic model of Baldwin and Lomax<sup>7</sup> with the modified Degani-Schiff method for smooth surface crossflow separation<sup>18</sup>.

In common with most CFD codes CHASM produces more accurate flowfield predictions when applied to meshes with comprise optimally orthogonal cells. Automatic generation of high resolution, high quality meshes for non specific geometries is complex and the subject of ongoing research worldwide. To produce satisfactory three-dimensional meshes for the generic geometry a four-stage process is employed.

Firstly the boundary  $j=1$  is generated which spans the length of the body along the surface for a specific  $\phi$ . This can be done either by knowing the analytic equation of the surface generator, or by interpolating discrete data points defining the surface.

Choosing  $j=j_{\max}$  to be suitably distant from the centerline, i.e to contain shock waves within the grid, setting the planes  $i=1$  and  $i=i_{\max}$  to be perpendicular to the centerline completes the definition of the boundaries of the physical domain for the mesh slice. Subdivision of each boundary into the required number of elements and applying transfinite interpolation produces a distributed set of points within the physical domain.

Geometric stretching is applied in both the  $x$  and  $y$  directions to the boundary points prior to transfinite interpolation to cluster cells near to the nose and surface of the body. To optimize the mesh in terms of orthogonality Thomas-Middlecoff functions<sup>19</sup> are applied and the resulting set of equations is solved iteratively using successive under relaxation. It should be noted, however, that the mesh is not orthogonal to the wall in the  $y$ -direction, particularly in the nose region.

A two dimensional slice through the mesh for the experimental model at  $\phi = 0$  is shown in Figure 2.

In this way, producing slices at each required  $\phi$  rotating about the centerline by  $\Delta\phi$  and assembling generates the required mesh.

Mesh convergence was assured through progressive increasing of the number of cells in the  $i$ ,  $j$  and  $k$  directions until the solution was found to be mesh independent, in terms of forces and moments. A mesh of 262,000 cells (65x65x65 vertices) was found to provide sufficient resolution for static analyses although the majority of the solutions were carried out with grids of 128x64x64 cells.

Convergence criteria were set at three orders of magnitude in the R2 norm for each primitive variable in each cross flow plane. Note that this cannot be easily compared with a time marching

analysis, since the initial solution at each cross flow plane is extrapolated from the "good" solution at the previous streamwise station.

A typical mesh of 128x64x64 cells could be generated in less than two minutes on a Sun Ultra ii workstation with a 350MHz processor. Solution times varied from 20 minutes to 50 minutes. The solution times increased with Mach number and angle of attack, because of the stronger flow gradients inhibiting convergence.

#### *ARL Numerical Predictions – CFD++ and ZNSFLOW*

Computational fluid dynamics approaches were used to compute the supersonic flow fields and aerodynamic forces and moments on H-series projectiles. Numerical solutions were obtained using the Navier-Stokes technique. Pitch-plane symmetry was used for all the computations. Viscous flow solutions were obtained using two Navier-Stokes flow solvers (ZNSFLOW<sup>20</sup> and CFD++<sup>21,22</sup>). Calculations for the H3P78 projectile were performed using both ZNSFLOW and CFD++ code at Mach 4.0 and several angles of attack from 0° to 12° for the wind-tunnel conditions, and  $M=4$ ,  $\alpha = 0$  and  $M=4.5$ ,  $\alpha = 6$  for sea-level free flight conditions

ZNSFLOW is a multi-block/Chimera<sup>23</sup> Navier-Stokes flow solver and uses an implicit, approximately factored scheme to solve the time-dependent Navier-Stokes equations using an upwind scheme in the streamwise direction and central differencing in the other two directions. For computation of turbulent flows, this code provides an algebraic Baldwin-Lomax<sup>24</sup> model and both one-equation and two-equation pointwise turbulence models. Computed results have been obtained for the H3P78 projectile at Mach 4 for the wind-tunnel conditions at various angles of attack as well as a free-flight condition at 0° angle of attack. In all these runs, the algebraic Baldwin-Lomax turbulence model was used to provide the turbulence closure.

CFD++ is a commercially available finite-volume time-dependent Navier-Stokes solver. It uses an unified-grid, unified-physics and unified-computing framework. Unsteady compressible and incompressible Navier-Stokes equations and wall-distance free pointwise turbulence models are solved on either structured, unstructured grids, or hybrid grids using TVD discretization based on a multi-dimensional interpolation framework and Riemann solvers. Computed results have been obtained for the H3P78 projectile at Mach 4 for the wind-tunnel conditions at various angles of attack as well as  $M=4$ ,  $\alpha = 0$  and  $M=4.5$ ,  $\alpha = 6$  for sea-level free flight conditions. In all these runs, a two-equation

pointwise k- $\epsilon$  turbulence model<sup>25</sup> was used to provide the turbulence closure.

A structured H-grid, shown in Figure 3 was used for both codes. Flowfield symmetry was assumed, so only half of the geometry was modeled. The total number of cells was 1.8 million, with an average first  $y^+$  of around 0.5. The grids took approximately one to two days to generate. Convergence was assumed when the residuals dropped by three to four orders of magnitude. The runs took about eight hours on 16 processors of an SGI O2. For more details on the grid and computations, see Sahu et al<sup>26</sup>.

### *Cobalt<sub>60</sub>*

Flow fields for the H3P78 configuration were computed using the Sep 2000 version of the Cobalt<sub>60</sub> code that had been developed by the Computational Sciences Branch at the U. S. Air Force Research Laboratory<sup>27</sup>. Cobalt<sub>60</sub> is an implicit, parallel code that can be used to solve the Navier-Stokes or Euler Equations. Reynolds-averaged turbulence models available in this version were: Spalart-Allmaras<sup>28</sup>, Menter's Baseline<sup>29</sup>, Menter's Shear Stress Transport<sup>29</sup>, and Wilcox's 1998  $k-\omega$ <sup>30</sup> models. Forsythe et al<sup>31</sup> tested these models on numerous benchmark cases, including a Mach 2.5 axisymmetric base flow. Menter's Baseline Model with compressibility correction was used for all the current calculations based on its performance in the base flow test case.

The unstructured grids that were used for the present study were generated using VGRIDns<sup>32</sup>. In order to minimize the computational resources required, the grid generation strategy took advantage of flow-field symmetry. For the zero degree case, only one quarter of the geometry was gridded, as shown in Figure 4. For the angle of attack cases, the grid was mirrored using the blacksmith utility<sup>33</sup> to provide a grid that modeled half of the geometry. This same process was applied for the beta cases. The quarter geometry grid contained 2.1 million cells while the half geometry grids contained 4.2 million cells. Prisms were used in the boundary layer, with an average first  $y^+$  of less than 0.2 and a geometric stretching growth rate of 1.25. Generation of the grid took approximately one day.

The far-field boundaries were located far enough from the surface of the model such that the entire bow-shock wave would be captured. The downstream boundary was located far enough downstream from the base to recover to supersonic flow thereby preventing any reflections at the downstream boundary from affecting the solution upstream.

Axial and normal forces, number of supersonic cells, and average first  $y^+$  values were monitored during the runs to check for convergence. The run was considered converged when these values changed by less than 1% over 500 iterations in a row. This approach required approximately 4000 iterations. On a 64 processor linux cluster with 500MHz PIII processors, this required about a day per run. A grid refinement study was not conducted previously, however, sensitivity to grid resolution was explored for the forebody region only<sup>34</sup>. A coarser grid than the current one was seen to give grid independent solutions for the pressures at two axial locations. This is certainly not proof of a grid converged solution for the current study, especially in the base region.

## **Results & Discussions**

For all coefficient, the reference length is the major ellipse diameter ( $d_{maj}$ ) of the base and the reference area is the cross section area of the model base ( $A = p * d_{maj} * d_{min}$ ). The moment reference point is about the nose. For the CFD codes, the forces and moments were a result of surface integration of the pressure and shear stress.

### *Comparison to Wind Tunnel Data*

The wind tunnel data of Orchard et al.<sup>6</sup> was used as a basis for comparison. Force and moment measurements of a full scale model were taken from Mach 2.5 to 4.0 at various roll angles. Computations were performed at Mach 4.0, matching the wind tunnel conditions, resulting in a Reynolds number based upon model length of  $1.9 \times 10^6$ . All codes performed an alpha sweep from 0 to 12 degrees. CHASM and Cobalt<sub>60</sub> were also run at varying sideslip (beta). The test matrix is shown in Table 1.

Code	Alpha	Beta
CHASM	0,2,4,6,8,10,12	0,2,4,6,8,10,12
CFD++	0,2,4,6,8,10,12	
Cobalt <sub>60</sub>	0,2,4,6,8,10,12	0,2,6,12
ZNSFLOW	0,4,8,12	

**Table 1.** CFD test matrix

To truly test the ability of CFD to function as a predictive tool, the computations for all codes were performed blind – i.e. without access to the experimental data.

The normal force vs. angle-of-attack is plotted in Figure 5. The two lines through the experimental data represent positive and negative angles of attack. There are only slight differences in the two lines showing good model/flow symmetry.

All codes do a good job predicting the normal force throughout the angle-of-attack range, falling within a few percent of the experimental data.

Pitching moment about the nose is next shown in Figure 6. Again, the agreement is quite good, with the exception of CHASM at 10 degrees. This point seems anomalous when compared to 8 and 12 degrees, where the agreement is better. The reason for this anomalous point is unknown. It is also noted that CHASM predicts a slightly lower (more negative) moment coefficients than the other codes, although the agreement to the experiments is just as close.

Using the normal force and pitching moment about the nose, a center of pressure was calculated for each angle of attack using:

$$\frac{x_{c.p.}}{l} = -\frac{C_m}{C_z} \frac{d_{ref}}{l} \quad (1)$$

Results are plotted in Figure 8. Since Equation (1) is indeterminate for zero normal force, zero degree results were excluded from this plot. The agreement is good for all codes but CHASM. It should be pointed out, however, that the scale has been expanded to highlight small differences. CHASM predicts a center of pressure location about 7% too far aft. The grid used for CHASM is coarser than the other grids, so grid resolution could possibly be a factor. The drop in center of pressure location approaching zero angle-of-attack in the experiments is troubling, since this would mean a reduction in stability at the lower angles. However, Equation 1 is very sensitive to small errors in the normal force for low angles, so it is not clear that this drop is physical.

The axial force coefficient is plotted in Figure 7. Results are plotted including and excluding the base. The wind tunnel model included a sting, while all CFD computations were made without a sting. Since CHASM is a PNS code, the effects of the base were not included. To remove the effects of the base in the wind tunnel results, base pressure was measured with static pressure taps. This pressure was then assumed to act over the entire base area. The resultant force was then subtracted from the axial force results, and replaced with freestream static pressure acting over the base. A similar procedure was used for the CFD results, except the force on the base was obtained by integrating pressure over the base.

The prediction of axial force including the base for the codes agreed fairly well with the experimental data. This is not entirely to be expected, however, since the wind tunnel model has a sting, while the computations do not. The experimental data show an increase in axial force at lower angles, which is not reproduced by any code.

There seems to be more scatter in the CFD data for the axial force than there was for the normal forces and moments. This may be due to the fact that the base pressure is sensitive to the turbulence modeling treatment.

The axial force coefficient excluding the base shows less scatter in the computations. The codes slightly under-predicts the axial force. Subtracting the base pressure, however, increased the scatter in the experimental data. This points to possible uncertainty in the experimental data.

Similar plots for varying sideslip angles are shown in Figures 9 through 11. The CHASM results were run on a very coarse grid - 33x33x65 and are most likely unresolved. The agreement for yaw force (Figure 9) and yaw moment (Figure 10) is good considering the low resolution. The center of pressure location shows quite a bit of scatter, however. The Cobalt<sub>60</sub> results are quite good for all parameters. The center of pressure location is predicted very accurately. The experimental center of pressure shows more asymmetry for the beta case than it did for the alpha. If the positive and negative beta lines were averaged, a reduction in the center of pressure location for small angles would result, just as in the alpha case. This trend is not duplicated in the CFD results.

#### *Comparison to Free Flight Data*

A limited number of free flight tests were conducted<sup>7</sup>. Unfortunately an insufficient number of shots were completed to provide accurate force and moment coefficients. However, three shots were completed providing estimated zero-yaw axial force coefficients at three Mach numbers.

Runs at standard day sea level conditions at Mach 4.0 were run using CFD++ and Cobalt<sub>60</sub>. The results are compared to the free flight runs in Figure 12. A linear curve fit is applied to the free flight data. Because of the limited amount of test points, and the scatter present at Mach 4.75, it is difficult to say very much meaningful about the CFD results. There are significant differences between the CFD results. The base drag for the three runs was fairly close, however. This means that the scatter is caused by the flow over the forebody. Further examination of the cause of this disagreement is required.

A single schlieren image was also obtained in free flight at Mach 4.53 – see Figure 13. There was no radar data to obtain exact roll and pitch angles. By visual inspection of the image, however, the pitch angle is around 6 degrees. The roll angle is more difficult to determine, but appears to be close to 45 degrees. CFD computations at 6 degrees alpha and zero degrees roll were performed using CFD++ and Cobalt<sub>60</sub> to make qualitative comparisons. Zero

roll was chosen to obtain a symmetric flow field, enabling a grid that only modeled half of the projectile.

From front to back are seen: the shock emanating from the nose of the vehicle, the shock from the flare, the expansion wave from the edge of the base, and the shear layer reattachment shock. The nose shock and the flare shock are seen to intersect aft of the vehicle in the windward plane in both the CFD and free flight images. The position of the reattachment shock also seems to be in close agreement to the flight test. The shear layer aft of the base is seen to be highly turbulent in the free flight case. The CFD results, since they are using Reynolds-averaged turbulence models produce a steady shear layer. The surface pressures for the CFD results show a local region of low pressure (blue) on the top of the forebody, which lies underneath a vortex that occurs even at this low angle of attack due to cross-flow separation.

### Conclusions

In summary, a comparison was made between several different CFD codes on a power-law elliptic section – the H3P78. Both experimental and flight test data were used, although the limited amount of flight test data prevented any significant conclusions. All CFD predictions were made “blind” to test the predictive capabilities of the codes for power-law elliptical projectiles.

All four codes adequately predicted the forces and moments on the projectile from 0 to 12 degrees. The center of pressure was well predicted, except in the case of CHASM, which might have more to do with grid resolution than the solver’s capability. Further examination in this area is required. No solvers predicted the slight decrease in center of pressure location for low angles. The most uncertainty in both the experimental and CFD results was seen in the axial force.

The results are not a conclusive validation study since a grid resolution study was not performed for most of the codes. Also surface pressures and wake data were not examined which would highlight more subtle features than integrated forces and moments. However the good agreement of four different codes on three different grids does build confidence in the use of CFD for design of slender projectiles. If used in true design mode, it would be extremely important to take much more caution in ensuring a grid-independent solution. Also it should be emphasized that great care was taken in selecting turbulence models that would well predict the base flow region, and the cross flow separation.

Also comments were made on the speed of the different codes. The code CHASM was by far the fastest since it solves the parabolized Navier Stokes equations. This makes this method extremely useful in the design phase where parametric studies of numerous shapes may need to be made. However, the drawback is the inability predict the axial force since the base drag is the predominant drag.

In terms of grid generation, CHASM was again the fastest since it has an automatic method of grid generation for projectiles. The geometry was simple enough that the unstructured grid (1 day to generate a grid) did not show a large advantage over the structured grid used for CFD++ and ZNSFLOW (1-2 days to generate a grid). However, the unstructured grid did have the advantage of not having extra cells at block interfaces near the farfield because of the restrictions of structured grids.

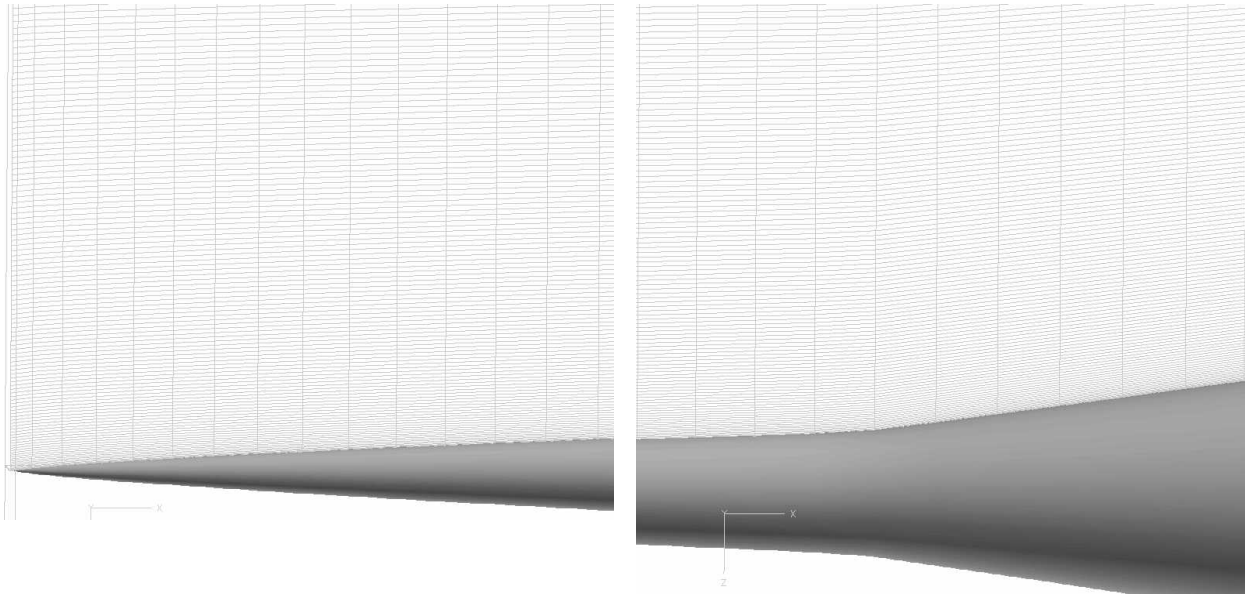
### *Acknowledgements*

The authors would like to acknowledge the help of Dr David Orchard of QinetiQ Ltd in assisting us with the wind tunnel data analysis. Also thanks go to Bill Strang of Cobalt Solutions, LLC for his help in the use of Cobalt<sub>60</sub>.

### References

- 1 Champigny, P and Lacau, RG, “Lateral Control Jets for Tactical Missiles,” Paper Number 3 in AGARD Report 804, Special Course, June 1994
- 2 Edwards, JA and Roper, JJ, “A Computational Assessment of Static and Dynamic Coefficients for the H3 Hypervelocity Projectile,” AIAA Paper 97-0640, Jan. 1997
- 3 Pagan, D, Molton, P, and Delery, J, “Basic Experiment on a Supersonic Vortex Flow Around a Missile Body,” Journal of Spacecraft and Rockets, Vol. 29, No. 3, May 1992, pp. 373-378
- 4 Grasso, F, and Iaccarino, G, “Influence of Crossflow and Turbulence on Vortex Flow Around a Supersonic Missile,” Journal of Spacecraft and Rockets, Vol. 35, No. 1, Jan.-Feb. 1998, pp. 37-45
- 5 Shereda, RE, Amidon, PF, and Dahlem, VI, “Wind-Tunnel Tests of Elliptic Missile Body Configurations at Mach Numbers 0.4 to 5.0,” AFWAL-TR-87-3086, Dec. 1987
- 6 Orchard, D., Fournier, E., Dupuis, A. and Edwards, J., “Wind Tunnel Tests on the H3P78, Power Law, Elliptic Section Flared Projectile from Mach 2.5 to 4,” AIAA 01-4321, Aug 2001.
- 7 Dupuis, A., Private Communication.

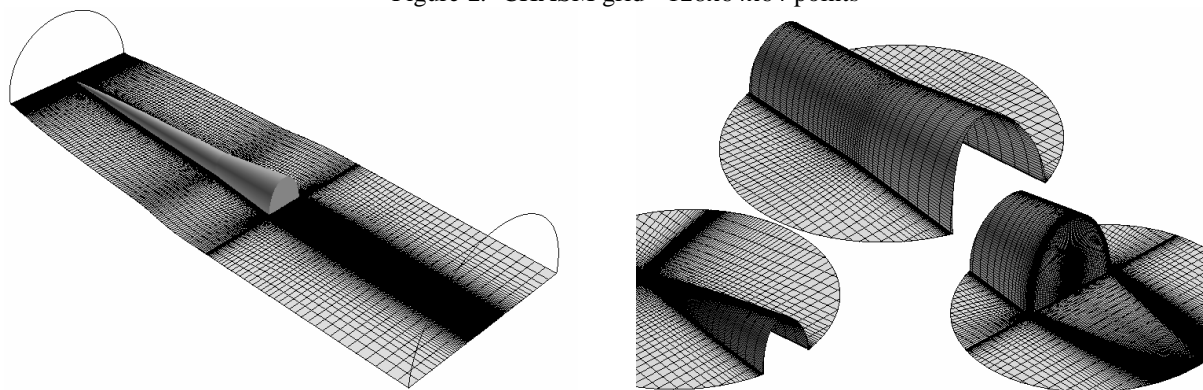
- 8 Birch, T., Qin, N. and Jin, X, "Computation of supersonic viscous flows around a slender body at incidence", AIAA Paper 94-1938, 1994
- 9 Qin, N., Ludlow, D., and Shaw, S., "Calculation of Pitch Damping Coefficients using the PNS Equations in a non-inertial framework", College of Aeronautics Report, March 1996.
- 10 Buckland, R. W., "Derivation of Aerodynamic damping coefficients from steady state flow computations", DRA Report TR-951157, March 1996.
- 11 Qin, N., Ludlow, D.K., Shaw, S. and Edwards, J. A., "Calculation of Pitch Damping Coefficients for projectiles", AIAA Paper 97-0405, 1997.
- 12 Edwards, J.A. and Roper, J.J., "A Computational Assessment of Static and Dynamic Coefficients for the H3 Hypervelocity Projectile", AIAA Paper 97-0640, 1997.
- 13 Birch, T.J., Prince, S.A., Ludlow, D.K., Qin, N. "The application of a parabolized Navier-Stokes solver to some hypersonic flow problems" AIAA Paper 2001-1753, 2001.
- 14 Prince, S. A., Williams, M. J. and Edwards, J.A. "Application of a Parabolized Navier-Stokes Solver to some problems in hypersonic propulsion aerodynamics", AIAA Paper 2001-4066, 2001
- 15 Osher, S. and Solomon, F., "Upwind difference schemes for hyperbolic systems of conservation laws", Maths. Comp., Vol 38, No. 158, 1982
- 16 Vigneron, Y. C., Rakich, J. V. and Tannehill, J. C., "Calculation of supersonic viscous flows over delta wings with sharp subsonic leading edges", AIAA Paper 78-1137, 1978.
- 17 Baldwin, B. and Lomax, H., "Thin layer approximation and algebraic model for separated turbulent flows", AIAA Paper 78-0257, 1978
- 18 Degani, D. and Schiff, B., "Computation of turbulent supersonic viscous flows around bodies having cross-flow separation", J. Comp. Physics, Vol 66, No 1, 1986
- 19 Thomas, P.D. and Middlecoff, J.F., "Direct control of the grid point distribution in meshes generated by elliptic equations", AIAA J., Vol 18, 1980
- 20 Edge. H.L., Sahu, J., Sturek, W.B., Pressel D.M., Heavey, K.R., Weinacht, P., Zoltani, C., Nietubicz, C.J., Clarke, J., Behr, M., and Collins, P., "CHSSI Computational Fluid Dynamics (CFD)-6 Project Final Report: ARL Block-Structured Gridding Zonal Navier-Stokes Flow (ZNSFLOW) Solver Software, ARL-TR-2084, February 2000.
- 21 O. Perroomian, S. Chakravarthy and U. Goldberg, "A 'Grid-Transparent' Methodology for CFD", AIAA Paper 97-07245, 1997.
- 22 O. Perroomian, S. Chakravarthy, S. Palaniswamy and U. Goldberg, "Convergence Acceleration for Unified-Grid Formulation using Preconditioned Implicit Relaxation", AIAA Paper 98-0116, 1998.
- 23 Steger, J. L., F. C. Dougherty, and J. A. Benek, "A Chimera Grid Scheme," Advances in Grid Generation, edited by K. N. Ghia and U. Ghia, ASME FED-5, June 1983.
- 24 Baldwin, B.L., H. Lomax, "Thin Layer Approximation and Algebraic model for Separated Turbulent Flows," AIAA 78-257, January 1978.
- 25 Goldberg, U.C., O. Perroomian, S. Chakravarthy, "A Wall-Distance-Free K-E Model With Enhanced Near-Wall Treatment," ASME Journal of Fluids Engineering, Vol. 120, pp. 457-462, 1998.
- 26 Sahu, J., Heavey, K.R., Edge, H.L., "Numerical Computations of Supersonic and Hypersonic Flow over Elliptic Projectiles," AIAA 01-3240, Aug, 2001.
- 27 Grismer, MJ, Strang, WZ, Tomaro, RF, and Witzeman, FC, "Cobalt, A Parallel, Implicit, Unstructured Euler/Navier-Stokes Solver," Advances in Engineering Software, Vol. 29, No. 3-6, 1998, pp. 365-373.
- 28 Spalart, PR, and Allmaras, SR, "A One-Equation Turbulence Model for Aerodynamic Flows," AIAA 92-0439, January 1992.
- 29 Menter, FR, "Zonal Two Equation  $k-\omega$  Turbulence Models for Aerodynamic Flows," AIAA 93-2906, 1993.
- 30 Wilcox, DC, Turbulence Modeling for CFD, Second Edition, DCW Industries, Inc., 1998.
- 31 Forsythe, JR, Strang, WZ, Hoffmann, KA, "Validation of Several Reynolds-Averaged Turbulence Models in a 3-D Unstructured Grid Code," AIAA 00-2552, June 2000.
- 32 Pirzadeh, S, "Three-Dimensional Unstructured Viscous Grids by the Advancing-Layers Methods," AIAA Journal, Vol. 34, No. 1, 1996, pp. 257-265.
- 33 <http://www.va.af.mil/vaa/vaac/COBALT/>
- 34 Schuricht, PH, Forsythe, JR, Bertin, JJ, and Abate, GL, "Comparison Between Measurements and Computations for Power-Law Elliptic Section Bodies," AIAA 00-2553, June 2000, Presented at Fluids 2000, Denver, CO



a) Mesh in the vicinity of the nose

b) Mesh in the vicinity of the flare junction

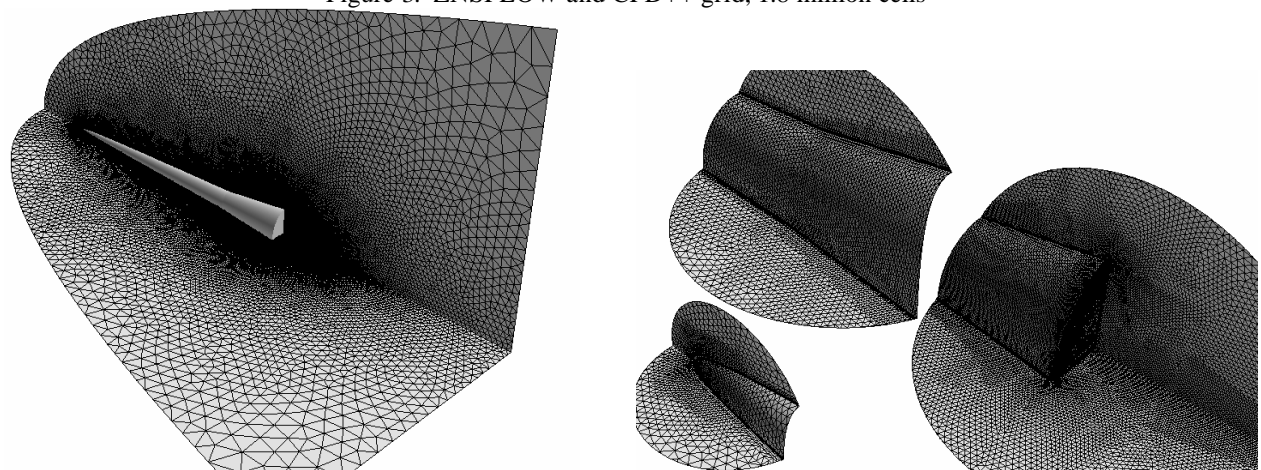
Figure 2. CHASM grid - 128x64x64 points



a) Mesh on the symmetry plane, and outline of in- and out-flow

b) Mesh in the vicinity of the nose, flare junction, and base

Figure 3. ZNSFLOW and CFD++ grid, 1.8 million cells



a) Mesh on the pitch and yaw planes

b) Mesh in the vicinity of the nose, flare junction, and base

Figure 4. Cobalt<sub>60</sub> grid - 1/4 of the geometry,  $2.1 \times 10^6$  cells

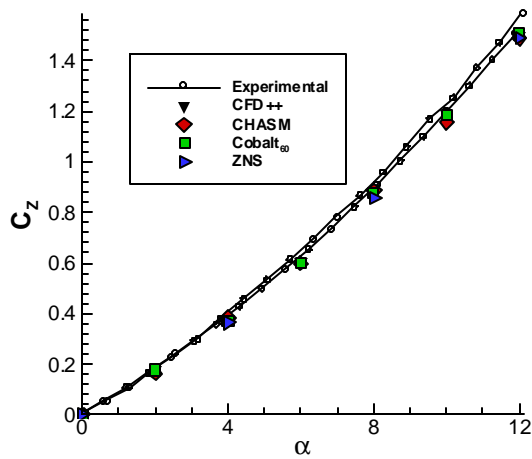


Figure 5. Normal force coefficient vs. alpha at M=4.0

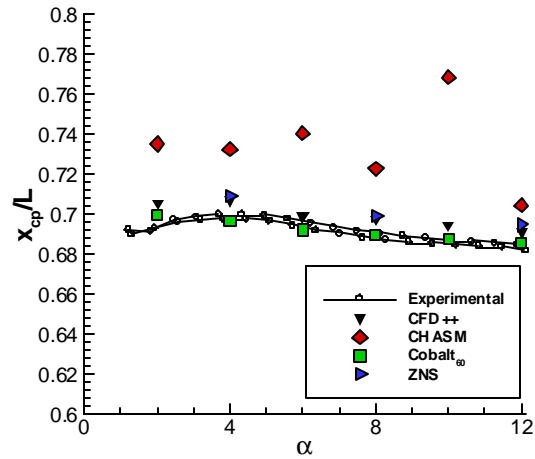


Figure 8. Center of pressure location vs. alpha at M=4.0

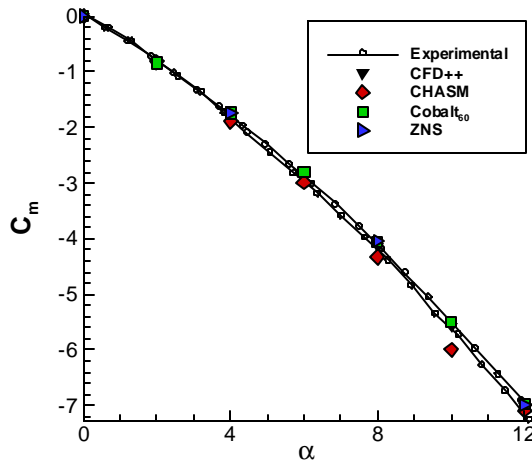


Figure 6. Pitching moment (about the nose) vs. alpha at M=4.0

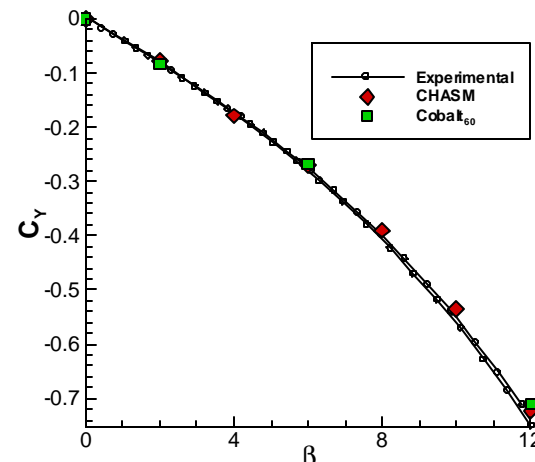


Figure 9. Yaw force vs. beta at M=4.0

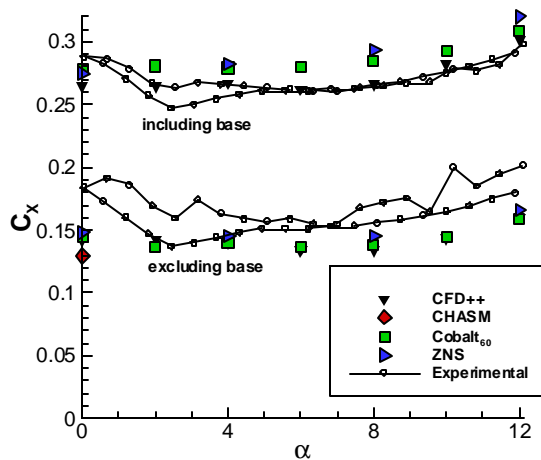


Figure 7. Axial force, with and without the base included at M=4.0

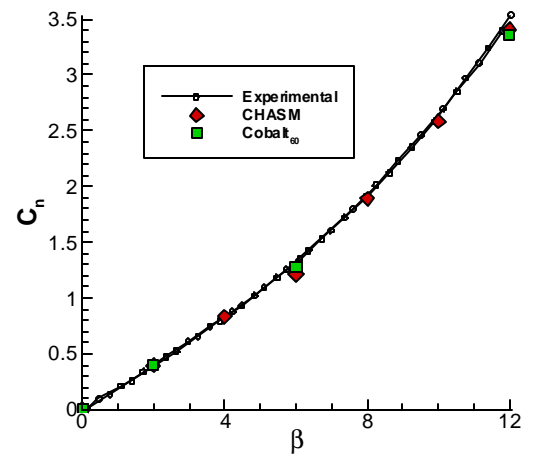


Figure 10. Yaw moment (about the nose) vs. beta at M=4.0

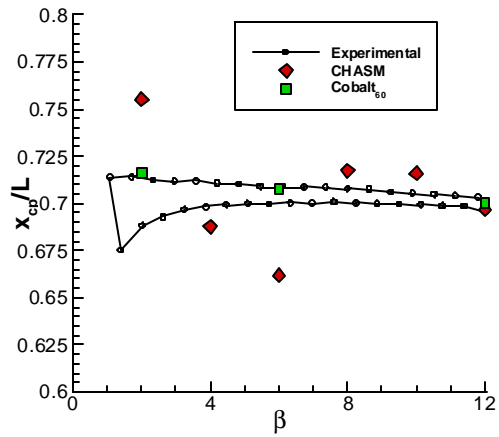


Figure 11. Center of pressure location vs. beta at M=4.0

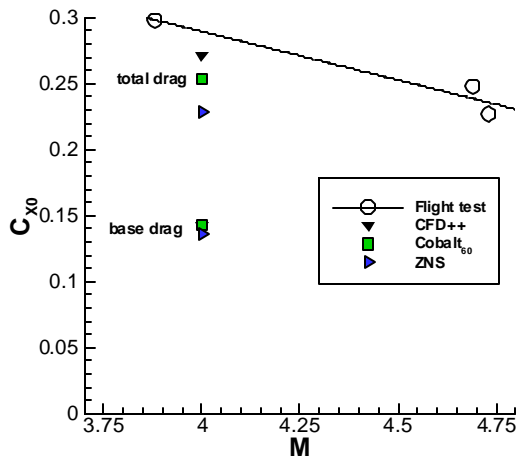


Figure 12. Zero yaw axial force coefficient vs. Mach number for free-flight conditions

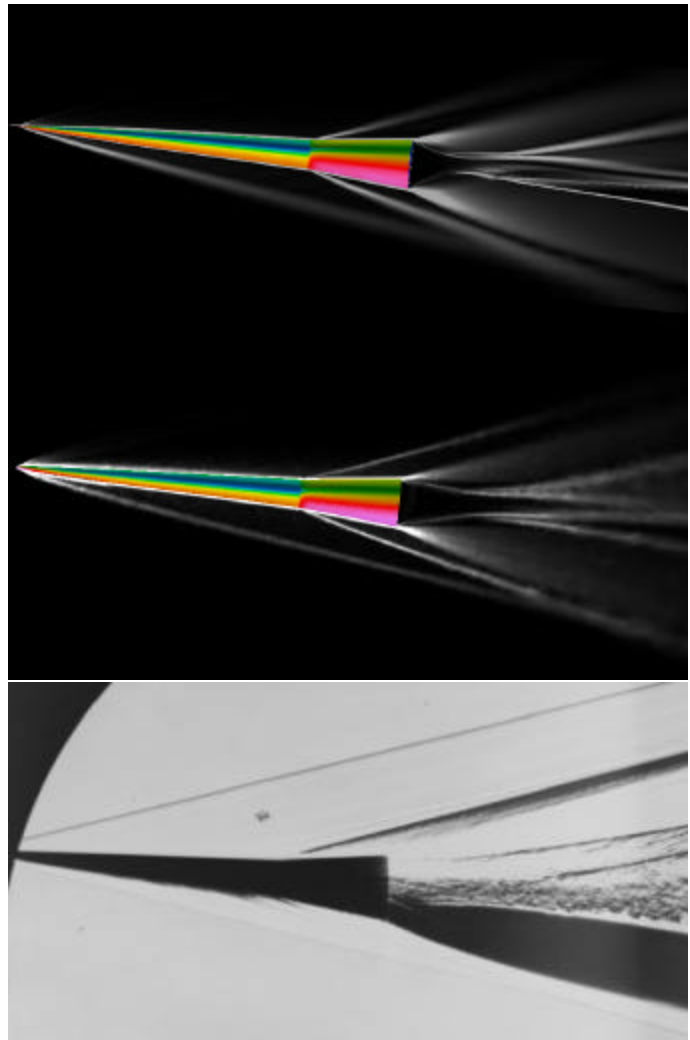


Figure 13. Comparisons of Schlierens at Mach 4.53 and 6° pitch. From top to bottom: CFD++, Cobalt60, flight test. CFD surface is colored by pressure. Roll angle of flight test model is unknown.